Journal of Materials Chemistry C

ROYAL SOCIETY OF CHEMISTRY

PAPER

View Article Online
View Journal | View Issue

Cite this: J. Mater. Chem. C, 2024, 12, 3365

Phosphine oxide based semiconducting small molecule as an additive and an electron transport layer enables efficient and stable perovskite light-emitting devices†

Susmita Mukherjee,[a] Ashutosh Panigrahi,[a] Yen-Hung Lin[b] and Ajay Perumal*[a]

Received 4th December 2023,
Accepted 25th January 2024

DOI: 10.1039/d3tc04461k

rsc.li/materials-c

Perovskite-based light-emitting diodes (Pe-LEDs) incorporate metal halide perovskites as the emissive layer in the form of polycrystalline thin films. Controlling the swift crystallization of these films poses challenges. However, the inclusion of phosphine oxide-derived additives during crystallization tempers this rapidity, yielding finer perovskite grains. This research studies how the type of phosphine oxide additive, be it insulating or semiconducting, modulates the optoelectronic characteristics of the methylammonium lead bromide ($MAPbBr_3$) perovskite layer, employing a nanocrystal pinning methodology. Comparing the semiconductor additive [2,4,6-tris[3-(diphenylphosphinyl)phenyl]-1,3,5-triazine] (PO-T2T) with the insulating tri-octyl phosphine oxide (TOPO) revealed that the former ensures steadier photoluminescence across varying conditions. Optimized Pe-LED devices with PO-T2T outperform their counterparts in multiple aspects, including reproducibility, low turn-on voltage (2.2 V), brightness (20 300 cd m^{-2}), efficiency (20.4 cd A^{-1}, 11.5 lm W^{-1} and 4.4%), and notably, prolonged electroluminescence (EL) duration compared to standard or TOPO-based Pe-LED devices.

Introduction

Metal halide perovskites (MHPs) have made rapid progress and shown tremendous potential in almost all optoelectronic devices such as LEDs,[1–4] solar cells,[5–8] photodetectors,[9] transistors[10] and optically pumped lasers[11] due to their outstanding optoelectronic properties. Solution processed metal halide perovskites exhibit extraordinary optoelectronic properties that are advantageous for achieving efficient light emitting diodes (LEDs) such as high photoluminescence quantum yield (PLQY), wider tunable band gap from the visible to infrared region of the electromagnetic spectrum (400–1000 nm), and narrow full width half maximum (FWHM) (<20 nm) with an ultra-high color purity emission spectrum.[12–15] Room temperature Pe-LEDs were demonstrated in 2014.[1] Since then, impressive improvements in device efficiency have been made and Pe-LEDs currently have efficiencies similar to those of organic light emitting devices (OLEDs).[13,14] Despite their rapid progress in efficiency, often the efficiencies of Pe-LED devices so far reported are at low luminance and the electroluminescence (EL) lifetime of visible Pe-LEDs is significantly smaller. Thus, further progress in efficiency, stability, and reproducibility especially at high current densities are challenges that need to be overcome for commercialization.

Unlike inorganic semiconductors which employ high temperature and low vacuum for single or polycrystalline film growth, metal halide perovskites employ low temperature and solution processing often requires a nitrogen atmosphere for obtaining high quality polycrystalline films. Metal halide perovskites are usually solution processed at mild or room temperature resulting in polycrystalline films; hence defects are inevitable, and these defects play a significant role in their optoelectronic performance. Improvements in the Pe-LED device performance so far have been achieved through improving the metal halide perovskite film morphology/regulation of crystal growth,[16–19] defect passivation,[20,21] and dimensionality engineering.[22]

It is important to control the rapid crystallization of halide perovskite materials to achieve the required phase with controlled defects which are intrinsic to solution processing and to come up with effective strategies to mitigate defect passivation. Various strategies have been employed to minimize the surface, grain boundary and bulk defects during polycrystalline perovskite film formation.[16–18,20,21,23] The nanocrystal pinning approach is one amongst them where an insulating or semiconducting small

[a] Functional NANO and Opto-electronics Lab (FNOL), Department of Physical Sciences, Indian Institute of Science Education and Research (IISER), Berhampur-760010, Odisha, India. E-mail: ajay@iiserbpr.ac.in
[b] Department of Electronic and Computer Engineering, The Hong Kong University of Science and Technology (HKUST), Clear Water Bay, Kowloon, Hong Kong

† Electronic supplementary information (ESI) available. See DOI: https://doi.org/10.1039/d3tc04461k

molecule (as an additive) is dissolved in the non-polar solvent and this additive solution is dripped as an anti-solvent during perovskite film formation. This approach was first reported with the n-type semiconducting TPBi[2,2′,2″-(1,3,5-benzinetriyl)-tris(1-phenyl-1-*H*-benximidazole)] molecule[19] and was shown to reduce the polycrystalline grain size and effectively passivate the surface defects thereby increasing the PLQY and device performance.[19,24] Insulating molecules such as long alkyl chain substituted phosphine oxide TOPO [tri-octyl phosphine oxide]25 and DBPF [2,7-dibromop-9,9-bis(3′-diethoxylphosphorylpropyl)-fluorene][26] and the n-type semiconducting molecules with larger pi-conjugated systems such as BPhen [bathophenanthroline],[27] BCP [bathocuproine],[28] SPPO-13 [2,7-bis(diphenylphosphoryl)-9,9′-spirobifluorene],[29] and DPPO [diphenylphosphine oxide][30] have been employed during perovskite crystallization to suppress the defects, reduce the grain size and improve the PLQY and the Pe-LED device efficiency.

Although various molecular additives have been reported to improve the device efficiency, their influence on PL stability and EL lifetime has not been explored in detail. In this work, we show that the nature of phosphine oxide additive not only regulates the defects in metal halide film and its optoelectronic properties, but also results in a significant improvement of device efficiency and enhances the EL stability of Pe-LED devices. We have employed the n-type semiconducting PO-T2T [2,4,6-tris[3-(diphenylphosphinyl)phenyl]-1,3,5-triazine] molecule as a superior molecular additive during $MAPbBr_3$ crystallization for defect passivation, while it also acts as an efficient electron transport layer (ETL). We find that the optoelectronic properties and PL stability of the $MAPbBr_3$ emission layer with PO-T2T molecules as an additive during perovskite crystallization are superior in comparison to those when using TOPO molecules. TOPO molecules have been previously used as an additive for defect passivation in $CsPbBr_3$ emission layer-based Pe-LEDs.[25,31]

With the help of photoluminescence measurements monitored across varying conditions, we show that the perovskite film with PO-T2T as an additive has more stable PL emission *vs.* the perovskite film with TOPO as an additive due to fewer defects in the film. We also compare the performance of the Pe-LED device and its EL stability with TOPO and PO-T2T additives, and we find that the optimized Pe-LED devices with the PO-T2T additive and the electron transport layer show excellent reproducibility, low turn-on voltage (2.2 V), bright electroluminescence (20 300 cd m^{-2}), maximum current and power efficiency (20.4 cd A^{-1}, 11.5 lm W^{-1}) and maximum external quantum efficiency (EQE) of 4.4%, and more importantly prolonged EL lifetime duration when compared to TOPO based or control Pe-LED devices.

Results and discussion

The $MAPbBr_3$ thin film which acts as an emission layer in this work is formed by spin coating the blend solution of $PbBr_2$ and MABr in DMSO with a molar ratio of 1 : 1.1 M; during the spinning process a volatile non-polar solvent (anti-solvent) addition initiates random nucleation and crystallization. Subsequent mild annealing of the film drives rapid heterogeneous poly-crystallization with large grains. If we dissolve a small amount of semiconducting small molecule in an anti-solvent (as an additive) the resulting films are more homogeneous and have smaller polycrystalline grains.[24] The schematic of thin film formation and subsequent anti-solvent dripping and annealing steps is summarized in Fig. 1. The molecular structures of additives (during anti-solvent step) TOPO and PO-T2T along with coordination of the P═O moiety with uncoordinated lead is schematically shown in Fig. 1. We prepare $MAPbBr_3$ polycrystalline films with the following anti-solvent treatments: (i) neat toluene as control sample, (ii) TOPO (an insulator) molecule dissolved in an anti-solvent, and (iii) PO-T2T (semiconductor) molecules dissolved in an anti-solvent at 0.65 mg ml^{-1} concentration, resulting in an ~200 nm thick perovskite layer. Both TOPO and PO-T2T have the phosphine oxide group and act as passivating molecules; the P═O moiety in these molecules effectively coordinates with uncoordinated lead (Pb^{2+}) atoms.[22,25,29,32] The extent of P═O moiety interaction for these two additives with different components of perovskite precursors is investigated by Fourier transform infrared spectroscopy (FTIR) and nuclear magnetic resonance (NMR) measurements. FTIR spectra are shown in Fig. 2(a) and (b), the spectra for pure TOPO and PO-T2T molecules have prominent peaks at 1145 cm^{-1} and 1196 cm^{-1} wavenumbers corresponding to P═O stretching vibrations. The presence of $PbBr_2$ with either TOPO or PO-T2T molecule resulted in a slight peak shift of the P═O stretching vibration to lower wavenumbers, 1070 cm^{-1} for $PbBr_2$:TOPO and 1176 cm^{-1} for $PbBr_2$:PO-T2T. The peak shifts clearly suggest that there is interaction between the P═O moiety and the lead (Pb^{2+}) atoms; therefore passivation of lead defects occurs. The extent of peak shift is not the same for both additives due to the difference in strength of interaction between Pb^{2+} atoms and the P═O moiety. Fig. 2(c) and (d) are NMR spectra and the shift of the ^{31}P spectral feature recorded by dissolving the perovskite components in deuterated DMSO. The $PbBr_2$ and MABr solutions were added to pure TOPO or PO-T2T solutions. Significant peak shift is observed with the addition of $PbBr_2$ or MABr separately to pure TOPO or PO-T2T solutions. The observed peak shift is not consistent due to changes in the chemical environment of phosphorus nuclei in two different additives and different interactions of P═O moieties with different perovskite precursor components. The peak shift observed by the addition of MABr is attributed to the formation of additional hydrogen bonds between ammonium and TOPO or PO-T2T molecules.[22] Both FTIR and NMR results confirm Lewis acid and Lewis base chemical interactions wherein the uncoordinated lead atom (Pb^{2+}) and ammonium components (NH^{3+}) act as Lewis acids and the P═O group acts as the Lewis base and the interactions assist in achieving the defect passivation.[22,33]

The surface morphology of perovskite films is crucial for Pe-LED device performance; the effect of additive molecules during crystallization and their influence on surface morphology of films is investigated by scanning electron microscopy (SEM) and atomic force microscopy (AFM). We observe significant contrast between perovskite films coated on glass to perovskite

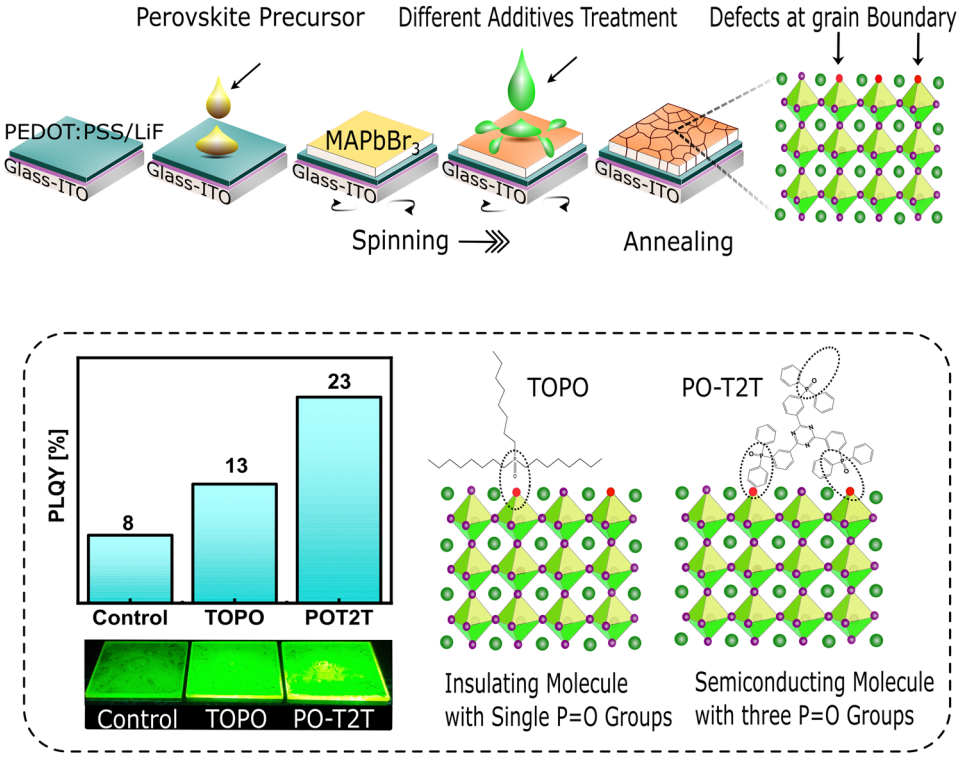

Fig. 1 Above: the schematic of thin film formation and subsequent anti-solvent dripping and annealing steps resulting in the polycrystalline perovskite phase. Below: the molecular structures of phosphine oxide bases additives (during the anti-solvent step) TOPO and PO-T2T and their coordination with uncoordinated lead atoms is illustrated.

films coated on a bare PEDOT:PSS hole transport layer (HTL) and a PEDOT:PSS/LiF modified HTL with 3 nm lithium fluoride (LiF). The perovskite film on glass [shown in Fig. S1(a) and (d), ESI†] has poor surface coverage with rough surface and pin holes, while the film deposited on a HTL/LiF is uniform, compact and highly crystalline with almost no pinholes as shown in Fig. [S1(c) and (f), ESI†]. The control film (with no additives) deposited on glass has a rough surface (feature heights of ~200 nm) and large polycrystalline domains having average crystalline domain size of ~330 nm. The same control film deposited on a HTL (PEDOT:PSS) has reduced crystalline domain size ~294 nm [Fig. S1(b), ESI†]. However, the photoluminescence (PL) emission of $MAPbBr_3$ is severely quenched on bare PEDOT:PSS HTL as shown in Fig. S2(a) and (b) (ESI†). The time resolved photoluminescence (TRPL) measurements performed on the same films and the TRPL decay profiles were fit with a tri-exponential function suggesting three-lifetime components, namely non-radiative bulk and surface traps with lifetime τ_1, τ_2 (fast-decay) and the radiative recombination inside the perovskite polycrystalline domains with lifetime τ_3 (slow-decay). A_1, A_2 and A_3 are the corresponding fractions of these components, the fitting parameters are tabulated in Table S1 (ESI†). The $MAPbBr_3$ film deposited on bare glass have much longer τ_{avg} of 35 ns; however for the perovskite films deposited on glass/HTL substrate we observe the lowest average lifetime τ_{avg} of 5.6 ns. The low τ_{avg} on glass/HTL substrate implies non-radiative exciton recombination being dominant in these films. The observed PL quenching of the $MAPbBr_3$ PL on the top of PEDOT:PSS is attributed to exciton dissociation due to the presence of traps and defects at the PEDOT:PSS/Perovskite interface. To mitigate the PL quenching, a thin layer of LiF as an interfacial layer was thermally deposited. The steady-state PL and time-resolved PL (TRPL) of $MAPbBr_3$ films on top of glass/HTL/LiF films are shown in Fig. S2 (ESI†). The improved PL intensity and exciton lifetime due to the addition of the LiF interfacial layer indicates a significant reduction in interface traps and defect density. All the parameters of fitted TRPL decays are summarised in Table S1 (ESI†). The morphology of the perovskite films is improved significantly with the addition of LiF. The polycrystalline domain size of the control film has reduced to ~160 nm on the top of PEDOT:PSS/LiF [shown in Fig. S1(c), ESI†]. More compact films without pin holes are formed on the PEDOT:PSS/LiF HTL compared to the PEDOT:PSS only HTL. The root-mean-square (RMS) roughness of $MAPbBr_3$ film measured in an AFM [Fig. S1(d)–(f), ESI†] for the HTL/LiF film is ~7 nm. Pinhole-free, smooth and compact $MAPbBr_3$ films are essential for efficient Pe-LED devices with lower leakage current. Hence, PEDOT:PSS/LiF [3 nm] was chosen to fabricate the devices after optimization. From here on for thin film characterization, we chose to deposit $MAPbBr_3$ films on HTL/LiF unless otherwise specified. Furthermore, we also observe stark contrast in the surface morphology investigated *via* SEM for the control and additive-based $MAPbBr_3$ films shown in Fig. 3(a)–(c). The inset in the figures shows the polycrystalline domain size distribution of the respective films. The average polycrystalline domain size is large for the

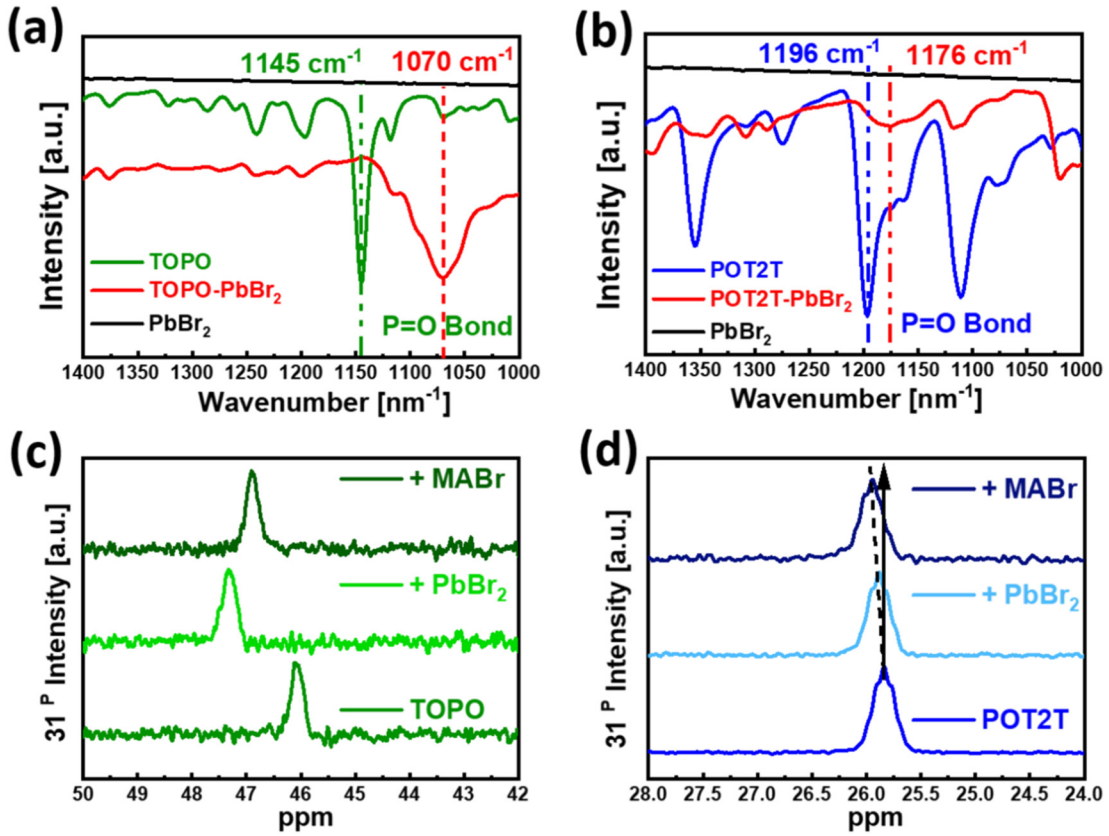

Fig. 2 (a) and (b) FTIR spectra of pure TOPO, pure PO-T2T, and pure $PbBr_2$ compared with FTIR spectra of TOPO and PO-T2T separately in the presence of $PbBr_2$. (c) and (d) ^{31}P NMR spectra of pure TOPO and pure PO-T2T compared with the ^{31}P NMR spectra of TOPO and PO-T2T in the presence of $PbBr_2$ and MABr separately.

$MAPbBr_3$ control film, ~160 nm, and the polycrystalline domain size decreases for $MAPbBr_3$ films with the TOPO additive to 126 nm and with the PO-T2T additive domain size further reduces to 74 nm and average rough surface features

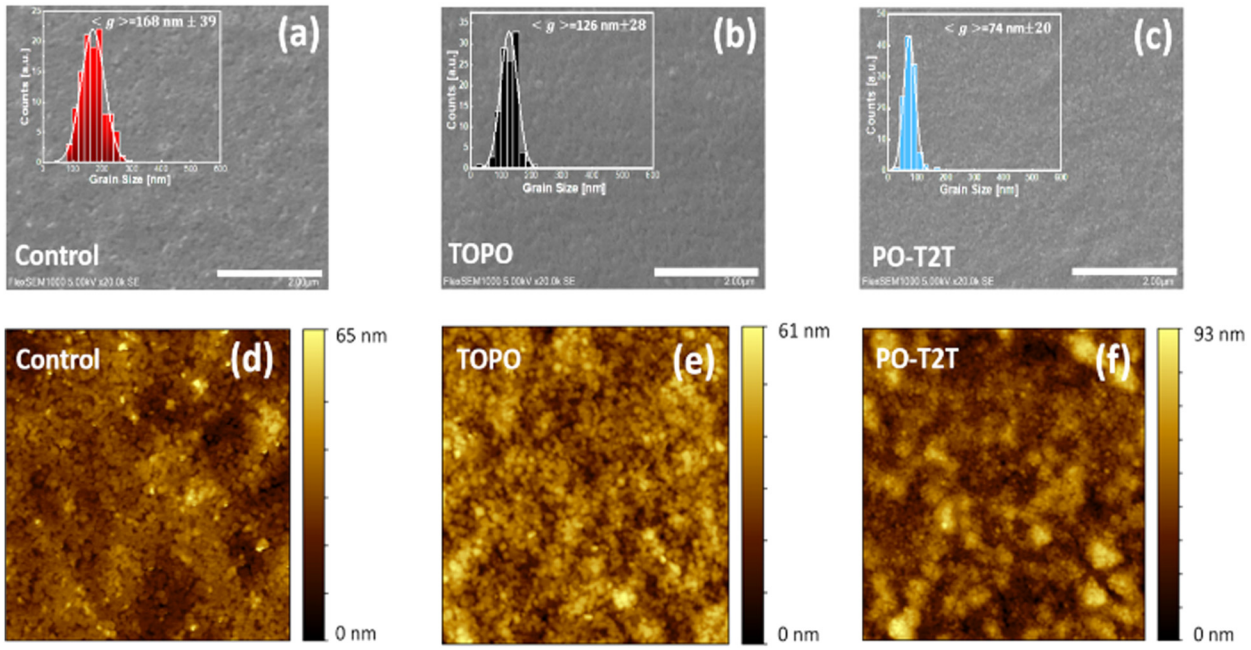

Fig. 3 SEM (above row) (a–c) and AFM images (below row) (d–f) of $MAPbBr_3$ films with control, TOPO and PO-T2T additives respectively. $MAPbBr_3$ films are prepared on a HTL (glass/PEDOT:PSS/3 nm LiF). The scale bar for SEM is 2 μm and the AFM images are of scan size 5 × 5 μm.

have a height of 60–90 nm. $MAPbBr_3$ films with the molecular additives show a more compact and homogeneous distribution of perovskite polycrystalline domains and they temper the rapidity of crystallization and regulate the growth of polycrystalline domains. More uniform, compact and smoother films are critical for achieving low leakage currents in multilayered Pe-LED devices.

X-ray diffraction (XRD) scans measured on $MAPbBr_3$ films deposited on a HTL/LiF are shown in Fig. S3 (ESI†). The control film (no additive) and the film with additive show similar perovskite crystalline phases. The XRD patterns have prominent diffraction peaks at 14.9°, 30.1°, and 45.9° assigned to the (100), (200), and (300) planes of cubic phase of $MAPbBr_3$ consistent with a cubic *Pm3m* space group phase.[34] The XRD patterns for $MAPbBr_3$ films with TOPO and PO-T2T molecular additives are identical (peak position, FWHM and lattice constant are almost the same) indicating that the small amount of additive molecules donot disrupt the perovskite crystalline phase or structure. The lattice constant is 5.9 Å and calculated film strain is lower for $MAPbBr_3$ with the PO-T2T additive. The XRD parameters from measurements are summarized in Table S2 (ESI†). Contact angle measurements confirm that the PEDOT:PSS film is hydrophilic with the water contact angle measured to be 30° as shown in Fig. S4 (ESI†). With LiF on the top of PEDOT:PSS HTL the water contact angle reduces to 22.5° indicating that the surface becomes more hydrophilic and the resulting perovskite films are continuous and pin hole free with higher surface coverage.

The optical properties of HTL/LiF/$MAPbBr_3$ control films (with no additive) and with molecular additives are shown in Fig. 4. Ultraviolet-visible (UV-VIS) absorption measurements of perovskite films deposited on HTL/LiF are shown in Fig. 4a. The absorption spectra for perovskite films with and without additives show distinct band edge excitonic features with peaks at 523 nm indicating that smaller crystalline grains are dominant in perovskite films and excitons are strongly confined to these smaller polycrystalline grains. The absorption spectra recorded for films with and without additives have similar absorption strength and onset indicating that the presence of a small number of additive molecules has no impact on crystalline structure or phase. The bandgap for these films was estimated by Tauc plot shown in the inset of Fig. 4a and is found to be 2.31 eV (with and without additives). Steady-state PL spectra of $MAPbBr_3$ perovskite films deposited on HTL/LiF are shown in Fig. 4b, the PL peak wavelengths are nearly the same for control, TOPO and PO-T2T additive perovskite films with PL emission spectra peaking at ~534 nm with FWHM of ~25 nm and PL intensity being greatly enhanced with additives as shown in Fig. 4b. The dominant peak in the PL emission

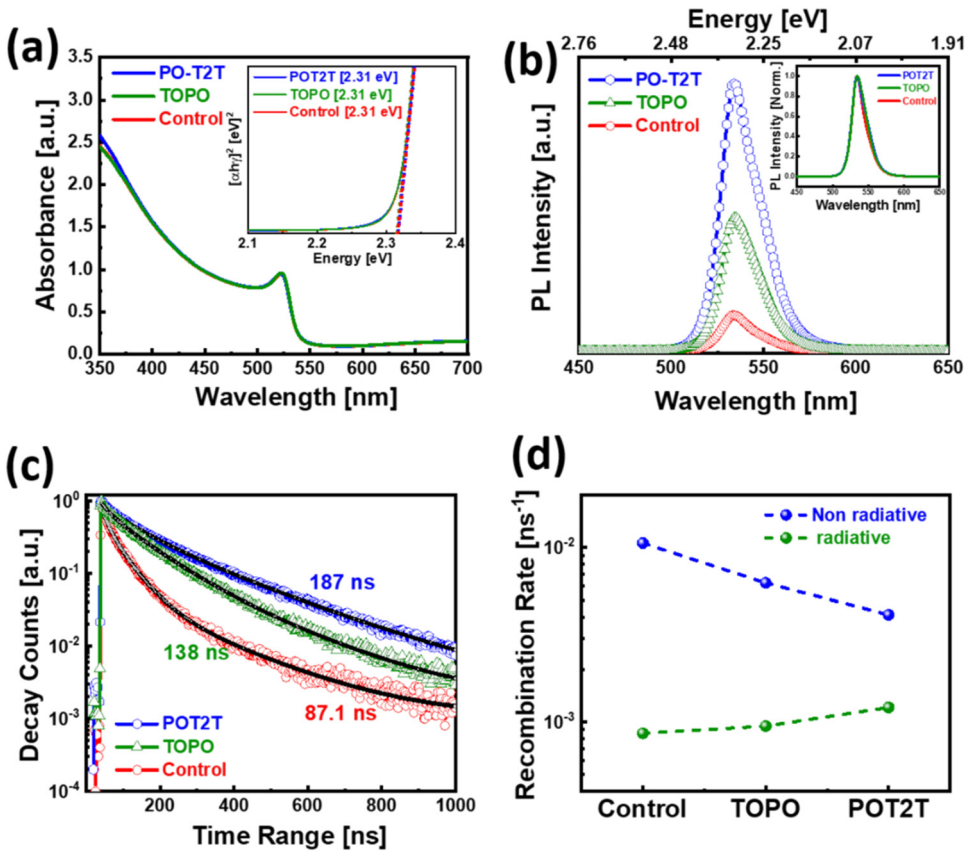

Fig. 4 (a) UV-Vis absorption spectra, (b) steady state PL spectra and (c) time resolved PL spectra and recombination rates for $MAPbBr_3$ films with control, TOPO and PO-T2T additives. (d) Radiative and non-radiative decay rates are calculated by using PLQY of films and TRPL decay curves. Perovskite films are prepared on a HTL for these measurements. Inset: (a) Band-gap estimation *via* Tauc plot and (b) PL peak intensity improvement *vs.* different additives.

spectra corresponding to ~534 nm is attributed to the bulk excitonic emission in agreement with the optical bandgap calculated from the Tauc plot shown in the inset of Fig. 4(a). We observe a shoulder peak in PL emission possibly attributed to the non-uniform size distribution of the polycrystalline material due to the size effect. The control perovskite film (no additive) has a PLQY of 8% while the perovskite films with TOPO and PO-T2T additives have PLQY of 13% and 23% respectively, clearly suggesting the influence of additives and their ability to passivate defects and suppress the non-radiative processes. Time resolved PL (TRPL) decay profiles of $MAPbBr_3$ perovskite films on HTL/LiF are shown in Fig. 4c and are fitted with a tri-exponential decay function, and the fit parameters are summarized in Table 1. For the control perovskite film the average lifetime is 87 ns, it increases to 138 ns for the perovskite film with the TOPO additive and the average lifetime almost triples to 187 ns for the perovskite film with the PO-T2T additive. The enhanced absolute PL intensity, PLQY coupled with prolonged PL average lifetime confirms that the presence of additives TOPO and PO-T2T during crystallization effectively lowers the non-radiative recombination sites in the perovskite film reducing the defect density and thereby increasing the radiative recombination.

The radiative and nonradiative recombination rate (k_r, k_{nr}) of the perovskite films is estimated using the equation

$$\text{PLQY} = k_r/(k_r + k_{nr}) \text{ and } \tau = 1/(k_r + k_{nr})$$

and is shown in Fig. 4d. The non-radiative rate k_{nr} decreases for $MAPbBr_3$ films with TOPO and PO-T2T passivation in comparison to control film. The radiative rate k_r is higher for films with TOPO or PO-T2T as additives. The higher absolute PL intensity, higher PLQY and higher average lifetime for films with TOPO and PO-T2T as additives in the $MAPbBr_3$ film clearly suggest better coordination of P═O with uncoordinated lead defects which reduces the non-radiative exciton decay processes.

Although metal halide perovskites have outstanding optoelectronic properties, often these properties are unstable and PL degradation is observed as a function of various external parameters due to the presence of defects and ion migration; therefore more often the Pe-LED devices are found to be short lived. To probe the influence of defects on the PL degradation in perovskite films, we measured a two dimensional (2D) PL spectral map as a function of time and temperature for control, TOPO and PO-T2T additive perovskite films as shown in Fig. 5 and Fig. S6 (ESI†).

In the control sample when PL emission is monitored as a function of time, we observe the PL emission spectral intensity reduction by ~80% from the initial value and the FWHM of the PL spectra broadens from 24 nm to 27 nm as shown in Fig. S5(a), S7(a) and S8(a) (ESI†). Temperature can also influence PL degradation by activating the non-radiative processes and accelerates the PL decay through thermal quenching. We probed the PL stability of perovskite films from room temperature (RT) up to 75 °C which we denote as high temperature (HT), as operating Pe-LEDs experience higher temperature due to Joule heating. The PL spectral emission intensity reduces by ~90% from the initial value at HT, the peak PL emission wavelength blue shifts from 533 nm at RT to 529 nm at HT and the FWHM of the PL emission spectra broadens from 25 nm to 27.5 nm as a function of temperature shown in Fig. S5(d), S7(d) and S8(d) (ESI†). The blue shift in emission maxima and the FWHM broadening of the emission spectra are attributed to exciton-phonon coupling.[35]

Table 1 Average lifetime calculated from a fitted tri-exponential decay model of films treated with different additives

Additive	τ_1 [ns]	B_1 [%]	τ_2 [ns]	B_2 [%]	τ_3 [ns]	B_3 [%]	τ_{ave} [ns]	χ^2
Control	15.94	12.30	52.05	60.09	195.5	27.61	87.21	0.951
TOPO	25.53	4.58	97.95	57.63	214.1	37.80	138.5	1.059
PO-T2T	25.58	2.50	94.73	30.02	235	67.48	187.6	0.900

XRD spectra recorded on the control film at RT and HT confirm the change in the lattice constant from 5.93 Å at RT to 5.96 Å at HT as shown in Fig. S9(j) (ESI†). A significant increment in the FWHM of PL spectra for the control films at elevated temperatures was observed [Fig. S7(d), ESI†]. This can be attributed to the strong exciton-phonon coupling at higher temperatures. We also observe a shift in peak emission wavelength [Fig. S8(d), ESI†] in the control sample which is due to change in the lattice constant observed from the relative change of the XRD peak position at higher temperatures as shown in Fig. S9(j), and Table S3 (ESI†) summarizes the parameters calculated from the XRD spectra.

In contrast, for the perovskite film with the TOPO additive the PL spectral emission intensity as a function of time reduces by 40% from the initial value with no change in either the emission peak wavelength or FWHM. At HT the PL spectral emission intensity reduces by 70% from the initial value as shown in Fig. S5(b), S7(b) and S8(b) (ESI†). With the PO-T2T additive the perovskite film exhibits maximum stability as the PL spectral emission intensity drops by only 20% from its initial value with no change in the peak emission wavelength or FWHM as a function of time. Even at HT the PL spectral intensity reduces only by 40% as shown in Fig. S5(c), S7(c) and S8(c) (ESI†).

The PL quenching observed in these films as a function of time or temperature is mainly attributed to the presence of defects and their diffusion due to ion transport[26] (formation energy for halide defects is known to be low) in halide perovskites[36,37] or it could be due to carrier trapping and excitation energy dissipation to the lattice vibrations. Thermal degradation can also cause instability of the perovskite structure resulting in the decrease of PL emission intensity at high temperatures. The XRD spectra recorded at HT shown in Fig. S9 (ESI†) confirm a very small change in the lattice constant which is unlikely to cause any lattice distortion; hence thermal quenching can be ruled out from structural rearrangement. Most likely the presence of additives during crystallization improves the thermal quenching of PL emission. The temperature in the form of the phonon can accelerate the ion diffusion and cause defect induced nonradiative recombination. The thermal quenching can also be likely due to difference in

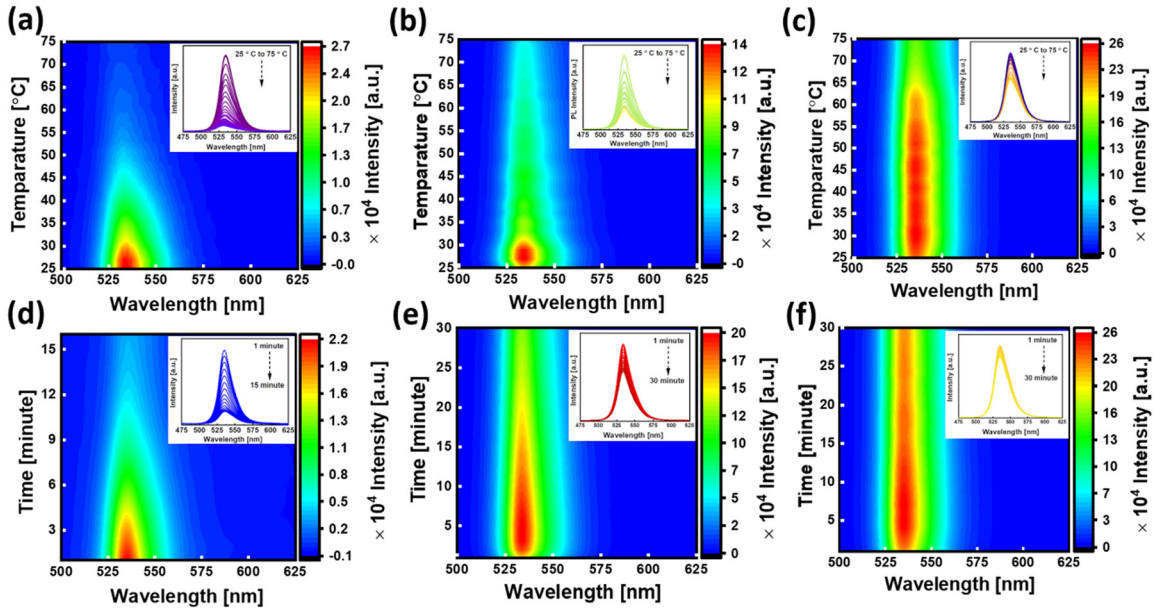

Fig. 5 Two-dimensional (2D) PL map of time (upper row (a)–(c)) and temperature (lower row (d)–(f)) dependent PL spectra of $MAPbBr_3$ films for control and film with TOPO and PO-T2T additives. $MAPbBr_3$ films were coated on the top of the HTL to retain the same morphology and conditions similar to the Pe-LED device sequence. Insets in (a)–(c) and (d)–(f): steady state PL profiles for $MAPbBr_3$ films *vs.* wavelength plotted as a function of time in the upper row and temperature in the lower row.

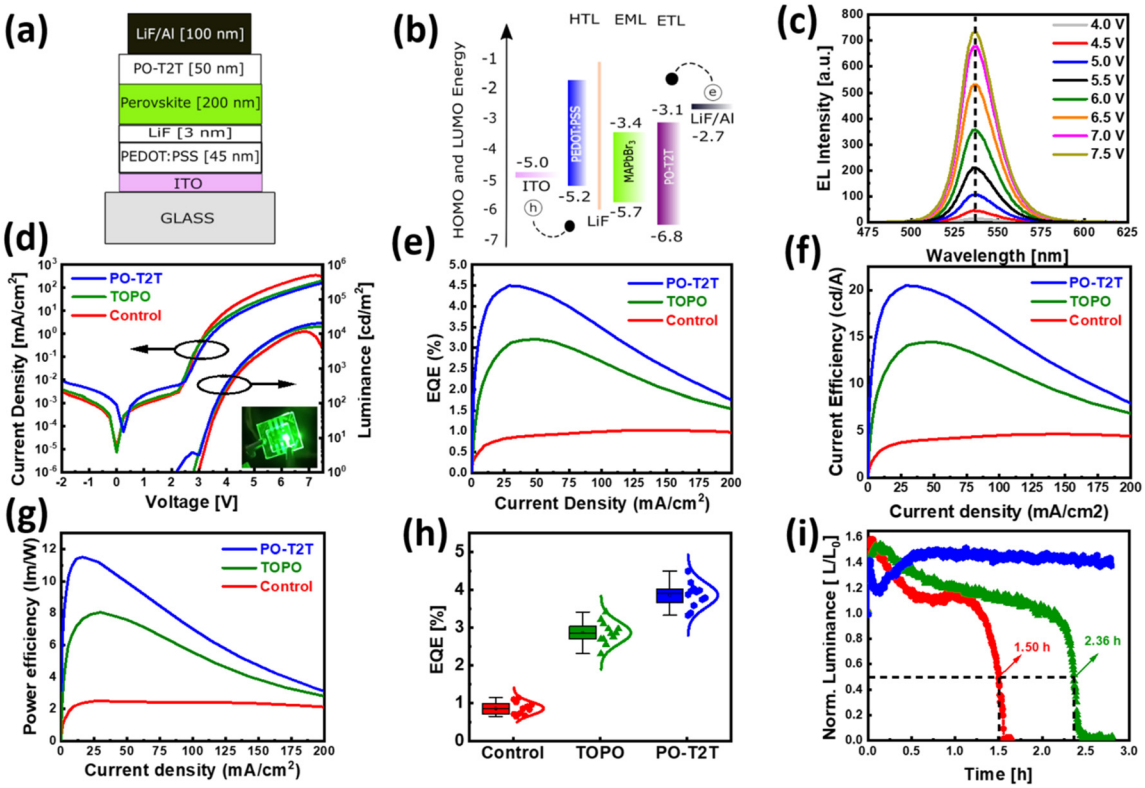

Fig. 6 Device structure and schematic energy level diagram of the component films are shown in (a) and (b) respectively. EL intensity emitted by the device as a function of wavelength at different voltages is shown in (c). [Inset shows the EL wavelength and FWHM are unchanged as a function of voltage]. Current density–voltage–luminance [*J*–*V*–*L*] characteristics of the device are shown in (d). EQE *vs.* current density is plotted in (e). Current efficiency *vs.* current density and power efficiency *vs.* current density of perovskite LEDs with different additives are shown in (f) and (g). (h) EQE histogram of 12 Pe-LED devices with control, TOPO and PO-T2T additives and (i) EL lifetime stability of Pe-LEDs with different additives.

carrier mobility and thermal conductivity between the two molecules. The PO-T2T molecule is more conductive (semiconducting) with a large pi-electron system in comparison to TOPO which is an insulator.

The promising optical properties of perovskite films combined with significantly improved PL stability encouraged us to integrate the perovskite film into efficient Pe-LED devices and study their EL stability. A schematic diagram of the bottom anode, bottom-emitting Pe-LED device architecture and the corresponding energy-level diagram for the component films is shown in Fig. 6(a) and (b); the energy levels were measured with an AC-2 photoelectron spectrometer in air shown in Fig. S10 (ESI†). We made Pe-LED devices with the device structure consisting of glass/ITO/PEDOT:PSS (40–45 nm)/LiF (3 nm)/$MAPbBr_3$ (180–200 nm)/PO-T2T (50 nm)/LiF ($\sim$2 nm)/Al (100 nm). The electroluminescence (EL) spectrum for the Pe-LED device with the PO-T2T additive is shown in Fig. 6(c). The EL peak has an emission maximum at 536 nm having a narrow FWHM of around 25 nm and the emission peak does not change with applied bias as shown in Fig. S11(b) and (c) (ESI†). The CIE coordinates for the EL emission spectra are (0.2, 0.7) and the EL spectra do not change with voltage bias as shown in Fig. S11(d) (ESI†). The CIE coordinates are closer to those of Rec. 2020 specified green emission, making them more attractive for high resolution display applications. Pe-LED devices reported in this work have an ultrathin layer of LiF on the top of the PEDOT:PSS HTL and the optimization of this layer is crucial for working Pe-LED devices as reported previously.[38,39] We have varied the thicknesses of the LiF film and optimized the Pe-LED devices for their performance as shown in Fig. S12 (ESI†). We find that a 3 nm thick LiF overlayer on PEDOT:PSS gives the best device performance and we have chosen this thickness of LiF for all devices. A higher thickness of LiF layer makes it insulating and reduces charge carrier injection and the device performance as summarized in Fig. S12 (ESI†). It also acts as a charge blocking layer for electrons, the electron confinement reduces the leakage current thereby improving the exciton recombination. We used PO-T2T as Electron Transport layer [ETL], which is well known in the OLED field as it has effective carrier mobility [$\sim 10^{-3}$ cm^2 V^{-1} s^{-1}] and deep HOMO [highest occupied molecular orbital] energy level [−6.8 eV] which helps in blocking the charge carriers from dissociating into the cathode. The current density–voltage–luminance (*J–V–L*) curves are shown in Fig. 6d. The control Pe-LED device has higher turn on voltage (3 V, determined as the driving voltage at $\sim$1 cd m^{-2}) and maximum luminance, current efficiency, power efficiency and EQE of 11 000 cd m^{-2}, 4.6 cd A^{-1}, 2.6 lm W^{-1} and 1% respectively. The control Pe-LED shows higher current density and lower luminance due to the higher hole mobility of $MAPbBr_3$ which is evident from current densities measured in hole only and electron only devices as shown in Fig. S13 (ESI†), the hole currents are an order of magnitude higher than electron currents. The hole carriers due to higher mobility are more likely to reach the electrode without forming the exciton hence the control device has lower brightness. The Pe-LED device with TOPO as an additive has a lower turn-on voltage (2.7 V) and improved maximum luminance, current efficiency, power efficiency and EQE of 16 200 cd m^{-2}, 14.4 cd A^{-1}, 8 lm W^{-1} and 3.2% respectively, and all the key device parameters are significantly higher than those of the control device. The TOPO molecule with its large bandgap, lower mobility and better morphology results in lower current density and higher luminance in comparison to the control device. The Pe-LED device with PO-T2T as an additive has the lowest turn on voltage of 2.2 V close to the bandgap of the emitter and significantly higher maximum luminance, current efficiency, power efficiency and EQE of 20 300 cd m^{-2}, 20.4 cd A^{-1}, 11.5 lm W^{-1} and 4.5% respectively, which is approximately 4.5 times higher than the performance of the control Pe-LED devices. The device performance plots are shown in Fig. 6(d)–(h) and the device performance comparison for control, TOPO and PO-T2T additive based Pe-LEDs is summarized in Table 2. The optimal molecular additive concentration is carefully chosen after optimizing the Pe-LED devices by varying the PO-T2T and TOPO concentrations in an anti-solvent during perovskite crystallization as shown in Fig. S14 and S15 (ESI†). We made statistics for EQE_{max} on the 12 devices for control, TOPO and PO-T2T additive based Pe-LED devices having excellent reproducibility with an average EQE_{max} of 0.85% for control, 2.85% for TOPO and 3.85% for PO-T2T based Pe-LED devices as shown in Fig. 6(h). We have calculated the standard deviation of EQE for the 12 individual devices. In the respective distribution, the standard deviations are 18.7%, 10%, and 8.1% respectively. This shows that additive-treated films have a lower deviation from the average and higher reproducibility in comparison to the control device. Other key parameters of the Pe-LED device and their distribution *e.g.* current and power efficiency, and luminance for control and additive based Pe-LED devices are given in Fig. S16 (ESI†).

We measured the EL operational stability of Pe-LED devices by monitoring EL intensity over time with the same initial luminance of 100 cd m^{-2} for all devices. The control Pe-LED device had the shortest T_{-50} lifetime of 1.5 h when the device was driven at a constant current density of 5.6 mA cm^{-2}, the Pe-LED devices with TOPO as the additive showed an improved T_{50}

Table 2 Summary of device performance. Device efficiency values are tabulated at 1 mA cm^{-2}, 10 mA cm^{-2}, and 100 mA cm^{-2}. Devices are driven at 100 cd m^{-2} for EL lifetime stability measurements

	Turn on voltage@ 1 cd m^{-2}	Luminance [cd m^{-2}]@ 1/10/100 mA cm^{-2}	EQE [%]@1/10/ 100 mA cm^{-2}	CE [cd A^{-1}]@1/ 10/100 mA cm^{-2}	PE [lm W^{-1}]@1/10/ 100 mA cm^{-2}	EL life time [L_{50} h] cd m^{-2}
Control	3.0	5.2/225/4040	0.28/0.65/1.00	1.09/3.0/3.5	0.96/2.2/2.4	1.50 h
TOPO	2.7	22.7/675/12015	0.62/2.3/2.7	3.23/10.3/12.0	2.78/6.9/5.6	2.36 h
PO-T2T	2.2	60.6/1977/17143	1.64/3.85/3.47	7.72/17.5/15.8	6.49/11.2/7.1	>3 h

lifetime of 2.3 h when the device was driven at a constant current density of 2.3 mA cm^{-2} while the Pe-LEDs with PO-T2T as an additive had much improved and higher T_{50} lifetime when the device is driven at a constant current density of 1.53 mA cm^{-2}. In addition, we also compared the EL lifetime of the $MAPbBr_3$-based [PO-T2T treated] device with conventional TPBi based ETLs. The EL lifetime of the PO-T2T-based ETL is superior compared to the TPBi based ETL device as shown in Fig. S17 (ESI†). To our knowledge the EL lifetime for PO-T2T is the highest for bulk $MAPbBr_3$ based Pe-LED devices reported in the literature so far and consistent with the much-improved thin film PL stability for the PO-T2T additive based perovskite film. These results clearly demonstrate the passivation strategy can effectively reduce the defect density and improve the device performance and significantly improve the operational stability of Pe-LEDs, crucial for their commercialization.

Conclusions

In summary, we show a correlation between passivation of uncoordinated Pb atoms and the PL stability. The chemical interaction of the P═O group with uncoordinated Pb atoms reduces the defect density thereby resulting in much improved optoelectronic properties and device performance. The nature of the phosphine oxide additive molecule also plays a significant role in regulating the defects which control the optoelectronic properties translating to significant improvement in the PL and EL stability in terms of longer operational lifetime and therefore more durable Pe-LED devices. Comparing the semiconductor additive PO-T2T with the insulating TOPO revealed that the former ensures steadier photoluminescence across varying conditions. We find that the optimized Pe-LED devices with the PO-T2T additive and electron transport layer have excellent reproducibility, low turn-on voltage (2.2 V), bright electroluminescence (20 300 cd m^{-2}), maximum current and power efficiency (20.4 cd A^{-1}, 11.5 lm W^{-1}) and maximum external quantum efficiency (EQE) of 4.4%, and more importantly, significantly longer electroluminescence (EL) lifetime when compared to TOPO based or control devices.

Experimental section

Materials

Prepatterned, semi-transparent indium doped tin oxide (ITO) film coated on glass substrates having a sheet resistance of 15 ohms sq^{-1} was sourced commercially. The poly(3,4-ethylenedioxythiophene:polystyrene sulphonate) commonly known as PEDOT-PSS (VP AL 4083) was procured from Heraeus Deutschland GmbH & Co. KG and used as a hole injection layer (HIL) and hole transport layer (HTL). Methylammonium bromide (MABr) was purchased from Great Cell Solar (Dyesol). Lead bromide ($PbBr_2$) was sourced from TCI chemicals. Toluene (anhydrous) and TOPO were purchased from Sigma-Aldrich. PO-T2T, TPBi and lithium fluoride (LiF) were purchased from Lumtec and were used as received.

Thin film and device fabrication

Glass or quartz substrates were used for optical characterization and pre-patterned ITO coated glass substrates were used for Pe-LED device fabrication. The substrates were cleaned in an ultrasonic bath for 15 minutes each by soaking them sequentially in soap solution, acetone, methanol, and isopropyl alcohol in that order. Clean substrates were subjected to oxygen plasma (150 W) for 15 min. Immediately the substrates were spin coated with the PEDOT:PSS polymer which was diluted in ethanol (2 : 1 v/v) and filtered through a 0.45 μm PVDF membrane before use. The PEDOT:PSS film coated substrates were annealed at 140 °C for 15 min in ambient air and the resulting films were approximately 40–45 nm in thickness. The ITO/PEDOT:PSS coated films were then transferred to a nitrogen filled glove box. A thin layer (3 nm) of lithium fluoride was evaporated in a thermal evaporator at 2×10^{-6} mbar vacuum. The substrates were then removed from the vacuum chamber and an emission layer was spin coated on the top of the LiF layer. The perovskite emission layer precursor preparation consists of dissolving MABr and $PbBr_2$ in a 1.1 : 1 M ratio (30 wt%) dissolved in DMSO at 60 °C for 4 hours. The perovskite precursor is spin coated on the substrates at 3000 rpm for 60 s, after 30 seconds of spinning 350 μl toluene [for control] or TOPO or PO-T2T dissolved in toluene is rapidly injected as an anti-solvent onto the spinning substrates. The substrates were annealed at 70 °C over a hot plate for 15 min resulting in 200 nm of perovskite emission layer. The substrates were transferred back to the thermal evaporator for coating TPBi (50 nm), LiF (2 nm), and aluminium (100 nm) sequentially in that order at a deposition rate of 0.5 Å s^{-1}, 0.3 Å s^{-1} and 1.5 Å s^{-1}. The devices were encapsulated inside the glove box (O_2 < 0.1 ppm, H_2O < 0.1 ppm) by a glass lid bonded *via* UV curing epoxy before being taken out of the glovebox for further characterization. The Pe-LED devices had an active area of 3 mm^2.

Thin film and device characterization

Film thickness is measured *via* a Dektak (Bruker) surface profilometer. Absorption spectra were recorded using a Shimadzu UV-VIS 2700 spectrometer. Steady-state photoluminescence (PL) and time resolved photoluminescence (TRPL) measurements were performed with a FLS 1000 (Edinburgh Instruments) spectrometer. The temperature dependent PL measurements were performed using a cryostat positioned at the sample holder position in the FLS 1000 spectrometer and samples were in a vacuum during measurement. For time-resolved PL (TRPL) measurements a pulsed excitation laser with 375 nm emission wavelength was used as the source. The PLQYs of thin films were determined using an integrated sphere. X-ray diffraction (XRD) patterns were obtained using a Mini flex benchtop X-ray diffractometer (Rigaku) having Cu-Kα radiation (λ = 1.54 Å). A table top SEM FlexSEM1000II from Hitachi was used to record SEM images. The nuclear magnetic resonance (NMR) spectra were recorded on a Bruker Avance Neo Ascend 400 MHz spectrometer. Fourier transform infrared

(FTIR) spectroscopy measurements were performed with a BRUKER TENSOR II system. The atomic force microscopy (AFM) measurements are performed using an OXFORD Instruments system in tapping mode. The roughness of samples was estimated using the Cypher S Igor pro 6 (OXFORD Instruments) software. The work function and highest occupied molecular orbital (HOMO) levels were measured using an AC-2 Riken Keiki photoelectron spectrometer in air. The current density–voltage–luminance characteristics of Pe-LED devices are measured using a fully automated assembly of a Keithley 2400 source meter, optical fiber coupled PMA-12 spectrometer to collect electroluminescence (EL) spectra while the device is mounted at the entrance port of an integrating sphere (C9920-12, Hamamatsu Photonics).

Conflicts of interest

There are no conflicts to declare.

Acknowledgements

A. P. acknowledges DST-SERB (ECRA/2019/000026, CRG/2022/009035) and IISER Berhampur (Initiation grant) for financial support. S. M. acknowledges IISER Berhampur for providing a PhD fellowship. A. Pa. acknowledges Inspire scheme support from DST Govt. of India.

Notes and references

1 Z.-K. Tan, R. S. Moghaddam, M. L. Lai, P. Docampo, R. Higler, F. Deschler, M. Price, A. Sadhanala, L. M. Pazos, D. Credgington, F. Hanusch, T. Bein, H. J. Snaith and R. H. Friend, *Nat. Nanotechnol.*, 2014, **9**, 687–692.
2 X. Y. Chin, A. Perumal, A. Bruno, N. Yantara, S. A. Veldhuis, L. Martínez-Sarti, B. Chandran, V. Chirvony, A. S.-Z. Lo, J. So, C. Soci, M. Grätzel, H. J. Bolink, N. Mathews and S. G. Mhaisalkar, *Energy Environ. Sci.*, 2018, **11**, 1770–1778.
3 Z. Wei, A. Perumal, R. Su, S. Sushant, J. Xing, Q. Zhang, S. T. Tan, H. V. Demir and Q. Xiong, *Nanoscale*, 2016, **8**, 18021–18026.
4 A. Perumal, S. Shendre, M. Li, Y. K. E. Tay, V. K. Sharma, S. Chen, Z. Wei, Q. Liu, Y. Gao, P. J. S. Buenconsejo, S. T. Tan, C. L. Gan, Q. Xiong, T. C. Sum and H. V. Demir, *Sci. Rep.*, 2016, **6**, 36733.
5 H. J. Snaith, *J. Phys. Chem. Lett.*, 2013, **4**, 3623–3630.
6 J. Y. Kim, J.-W. Lee, H. S. Jung, H. Shin and N.-G. Park, *Chem. Rev.*, 2020, **120**, 7867–7918.
7 H. Kim and N. Park, *Adv. Mater.*, 2023, **35**(43), DOI: **10.1002/adma.202204807**.
8 C. Ma and N.-G. Park, *Chem*, 2020, **6**, 1254–1264.
9 L. Dou, Y. Yang, J. You, Z. Hong, W.-H. Chang, G. Li and Y. Yang, *Nat. Commun.*, 2014, **5**, 5404.
10 Y. Lin, P. Pattanasattayavong and T. D. Anthopoulos, *Adv. Mater.*, 2017, **29**(46), DOI: **10.1002/adma.201702838**.
11 H. Zhu, Y. Fu, F. Meng, X. Wu, Z. Gong, Q. Ding, M. V. Gustafsson, M. T. Trinh, S. Jin and X.-Y. Zhu, *Nat. Mater.*, 2015, **14**, 636–642.
12 T.-H. Han, K. Y. Jang, Y. Dong, R. H. Friend, E. H. Sargent and T.-W. Lee, *Nat. Rev. Mater.*, 2022, **7**, 757–777.
13 X.-K. Liu, W. Xu, S. Bai, Y. Jin, J. Wang, R. H. Friend and F. Gao, *Nat. Mater.*, 2021, **20**, 10–21.
14 L. N. Quan, F. P. García de Arquer, R. P. Sabatini and E. H. Sargent, *Adv. Mater.*, 2018, **30**(45), DOI: **10.1002/adma.201801996**.
15 M. Saliba, J. Correa-Baena, M. Grätzel, A. Hagfeldt and A. Abate, *Angew. Chem., Int. Ed.*, 2018, **57**, 2554–2569.
16 Z. Xiao, R. A. Kerner, L. Zhao, N. L. Tran, K. M. Lee, T.-W. Koh, G. D. Scholes and B. P. Rand, *Nat. Photonics*, 2017, **11**, 108–115.
17 G. Li, Z.-K. Tan, D. Di, M. L. Lai, L. Jiang, J. H.-W. Lim, R. H. Friend and N. C. Greenham, *Nano Lett.*, 2015, **15**, 2640–2644.
18 B. Zhao, S. Bai, V. Kim, R. Lamboll, R. Shivanna, F. Auras, J. M. Richter, L. Yang, L. Dai, M. Alsari, X.-J. She, L. Liang, J. Zhang, S. Lilliu, P. Gao, H. J. Snaith, J. Wang, N. C. Greenham, R. H. Friend and D. Di, *Nat. Photonics*, 2018, **12**, 783–789.
19 H. Cho, S.-H. Jeong, M.-H. Park, Y.-H. Kim, C. Wolf, C.-L. Lee, J. H. Heo, A. Sadhanala, N. Myoung, S. Yoo, S. H. Im, R. H. Friend and T.-W. Lee, *Science*, 2015, **350**, 1222–1225.
20 S. Lee, D. Bin Kim, J. C. Yu, C. H. Jang, J. H. Park, B. R. Lee and M. H. Song, *Adv. Mater.*, 2019, **31**(20), DOI: **10.1002/adma.201805244**.
21 X. Shen, K. Kang, Z. Yu, W. H. Jeong, H. Choi, S. H. Park, S. D. Stranks, H. J. Snaith, R. H. Friend and B. R. Lee, *Joule*, 2023, **7**, 272–308.
22 D. Ma, K. Lin, Y. Dong, H. Choubisa, A. H. Proppe, D. Wu, Y.-K. Wang, B. Chen, P. Li, J. Z. Fan, F. Yuan, A. Johnston, Y. Liu, Y. Kang, Z.-H. Lu, Z. Wei and E. H. Sargent, *Nature*, 2021, **599**, 594–598.
23 J. Xue, R. Wang and Y. Yang, *Nat. Rev. Mater.*, 2020, **5**, 809–827.
24 M.-H. Park, S.-H. Jeong, H.-K. Seo, C. Wolf, Y.-H. Kim, H. Kim, J. Byun, J. S. Kim, H. Cho and T.-W. Lee, *Nano Energy*, 2017, **42**, 157–165.
25 X. Yang, X. Zhang, J. Deng, Z. Chu, Q. Jiang, J. Meng, P. Wang, L. Zhang, Z. Yin and J. You, *Nat. Commun.*, 2018, **9**, 570.
26 D. Zhang, Y. Fu, H. Zhan, C. Zhao, X. Gao, C. Qin and L. Wang, *Light: Sci. Appl.*, 2022, **11**, 69.
27 N. F. Jamaludin, N. Yantara, Y. F. Ng, A. Bruno, B. K. Chandran, X. Y. Chin, K. Thirumal, N. Mathews, C. Soci and S. Mhaisalkar, *J. Mater. Chem. C*, 2018, **6**, 2295–2302.
28 X. Sun, C. Han, K. Wang, H. Yu, J. Li, K. Lu, J. Qin, H. Yang, L. Deng, F. Zhao, Q. Yang and B. Hu, *ACS Appl. Energy Mater.*, 2018, **1**, 6992–6998.
29 M. Li, Y. Zhao, X. Qin, Q. Ma, J. Lu, K. Lin, P. Xu, Y. Li, W. Feng, W.-H. Zhang and Z. Wei, *Nano Lett.*, 2022, **22**, 2490–2496.

30 Y. Fu, H. Zhan, D. Zhang, Y. Cheng, L. Wang and C. Qin, *ACS Appl. Mater. Interfaces*, 2023, **15**, 10877–10884.
31 I. Schmidt, S. Olthof, H. Xu and K. Meerholz, *Adv. Opt. Mater.*, 2022, **10**(3), DOI: 10.1002/adom.202101602.
32 X. Chen, J. Huang, F. Gao and B. Xu, *Chem*, 2023, **9**, 562–575.
33 Y. Zhao, M. Li, X. Qin, P. Yang, W.-H. Zhang and Z. Wei, *ACS Appl. Mater. Interfaces*, 2023, **15**, 3644–3650.
34 F. Chen, C. Zhu, C. Xu, P. Fan, F. Qin, A. Gowri Manohari, J. Lu, Z. Shi, Q. Xu and A. Pan, *J. Mater. Chem. C*, 2017, **5**, 7739–7745.
35 A. D. Wright, C. Verdi, R. L. Milot, G. E. Eperon, M. A. Pérez-Osorio, H. J. Snaith, F. Giustino, M. B. Johnston and L. M. Herz, *Nat. Commun.*, 2016, **7**, 11755.
36 N. Phung, A. Mattoni, J. A. Smith, D. Skroblin, H. Köbler, L. Choubrac, J. Breternitz, J. Li, T. Unold, S. Schorr, C. Gollwitzer, I. G. Scheblykin, E. L. Unger, M. Saliba, S. Meloni, A. Abate and A. Merdasa, *Joule*, 2022, **6**, 2152–2174.
37 D. Meggiolaro, E. Mosconi and F. De Angelis, *ACS Energy Lett.*, 2019, **4**, 779–785.
38 B. Zhao, Y. Lian, L. Cui, G. Divitini, G. Kusch, E. Ruggeri, F. Auras, W. Li, D. Yang, B. Zhu, R. A. Oliver, J. L. MacManus-Driscoll, S. D. Stranks, D. Di and R. H. Friend, *Nat. Electron.*, 2020, **3**, 704–710.
39 Z. Liu, X. Xue, Z. Kang, R. Wang, H. Zhang and W. Ji, *Opt. Lett.*, 2021, **46**, 4378.